Supplementary Material: Spatial correlation between fluctuating and static fields over metal and dielectric substrates

Martin Héritier,[1] Raphael Pachlatko,[1] Ye Tao,[2] John M. Abendroth,[1] Christian L. Degen,[1] and Alexander Eichler[1,*]

[1]*Laboratory for Solid State Physics, ETH Zürich, CH-8093 Zürich, Switzerland.*

[2]*Rowland Institute at Harvard, 100 Edwin H. Land Blvd., Cambridge MA 02142, USA.*

(Dated: Monday 30th August, 2021)

S1. CANTILEVER CHARACTERIZATION

Details about the silicon nanoladder cantilever design were reported in a previous publication [S1]. In Fig. S1(a), we show the displacement power spectral density (PSD), measured at $4\,\mathrm{K}$, of the cantilever used in this study. We use such measurements at room temperature to calibrate the effective resonator mass m, and repeat them at cryogenic temperatures to verify the effective temperature T of the sensor. A typical ringdown experiment used to determine the Q-factor is displayed in Fig. S1(b). The driving power applied before each ringdown measurement was chosen such that the mechanical oscillations never exceeded $100\,\mathrm{nm}$ (to avoid nonlinearities in the detection scheme).

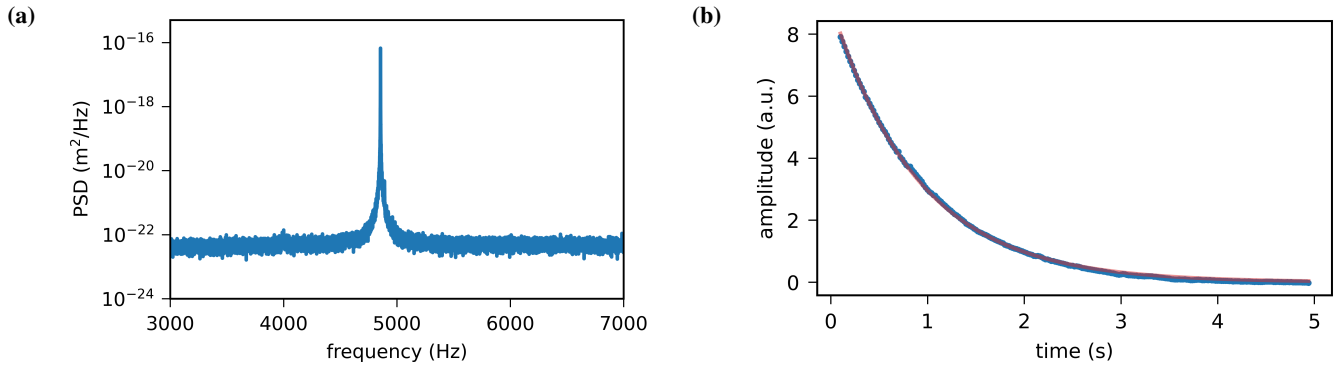

Figure S1: (a) Cantilever displacement power spectral density around its fundamental frequency of $4.858\,\mathrm{kHz}$ at $4\,\mathrm{K}$. (b) Typical cantilever ringdown measurement. The decay of the amplitude is averaged over $10-20$ runs and fitted by an exponential decay (red line).

S2. MODEL OF TWO DIELECTRIC LAYERS

In the main text, we use the model by Yazdanian et al. to calculate the non-contact friction due to dielectric fluctuations in thin adsorbant layers on Au and SiO_2 [S2]. The model assumes that the dielectric layer is directly supported by a metal, as is the case for our Au sample. For SiO_2, the situation is slightly different, as the adsorbant layer is supported by a second dielectric (SiO_2) whose influence we account for by an additive term in Γ_{NCF} that we calculate with the same equation, see dashed line in Fig. 3(c). We neglect the influence of the Si substrate that is more than $1\,\mu\mathrm{m}$ away from the tip.

A more rigorous way to calculate Γ_{NCF} for our SiO_2 sample is provided by the model by Lekkala et al. [S3]. In this model, a dielectric and a semiconducting layer are considered. By setting the density of free charges in the semiconductor to be zero, we arrive at a model for two dielectric layers.

*Electronic address: eichlera@phys.ethz.ch

The equation to calculate Γ_{NCF} with the Lekkala model is [S3]

$$\Gamma_{\mathrm{NCF}} = -\frac{q_{\mathrm{tip}}^2}{16\pi^2 f \epsilon_0} \int_0^\infty du u^2 e^{-2ud} \mathrm{Im}\left(\frac{\epsilon_c - \xi(u)}{\epsilon_c + \xi(u)}\right) \tag{S1}$$

Here, we use the definitions

$$\xi(u) = \frac{\sinh(uh)^2 + \alpha \cosh(uh)\sinh(uh)}{\alpha \sinh(uh)^2 + \cosh(uh)\sinh(uh)}\,, \tag{S2}$$

$$\alpha = \frac{\epsilon_c}{\epsilon_{\mathrm{SiO_2}}}\,, \tag{S3}$$

where $\epsilon_{\mathrm{SiO_2}}$ is the relative dielectric permittivity of the SiO_2 substrate and all other parameters are defined as in the main text. The results we obtain with this model, using identical values as in the main text, are shown in Fig. S2. We find a small quantitative difference compared to the Yazdanian model.

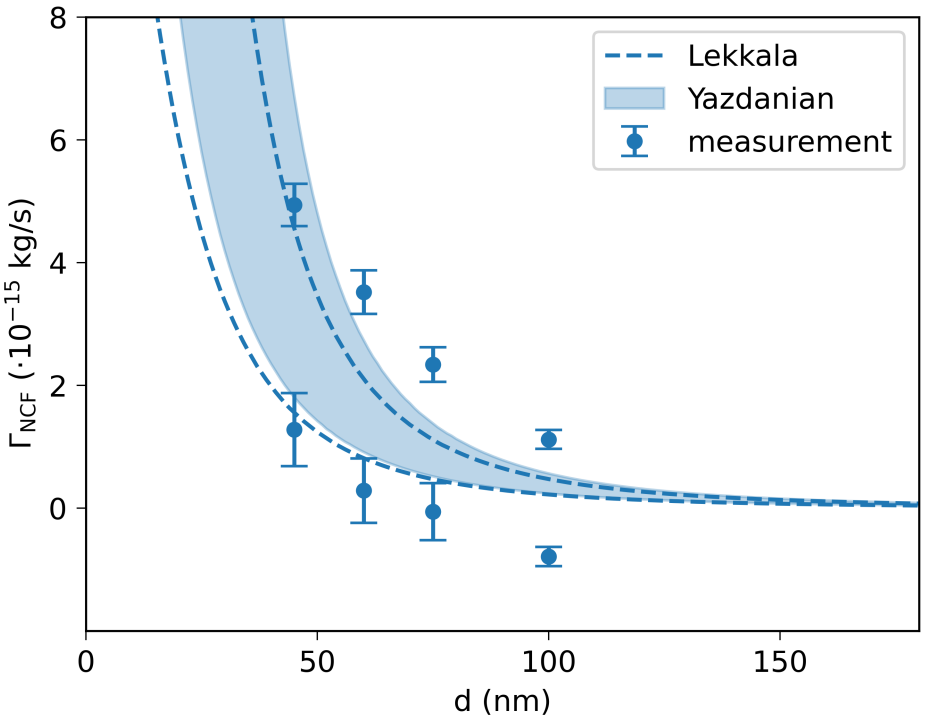

Figure S2: Comparison of the results for Γ_{NCF} of a dielectric layer with $\epsilon = 2$, $\tan\theta = 0.03$ and $0.4 < h < 2\,\mathrm{nm}$, over a $1.5\,\mu\mathrm{m}$-thick layer of SiO_2, calculated with the models by Yazdanian et al. [S2] and Lekkala et al. [S3].

S3. RESULTS WITH MAGNETIC FIELD

In this section, we present the data measured under an external magnetic field of $B = 4\,\mathrm{T}$ applied in the z-direction. At this field, the Boltzmann energy $k_{\mathrm{B}}T$ and the magnetic potential energy $\mu_{\mathrm{B}}B$ of electron spins are approximately equal, where $k_{\mathrm{B}} = 1.38 \times 10^{-23}\,\mathrm{J\,K^{-1}}$ is the Boltzmann constant, $T = 4\,\mathrm{K}$ is the temperature, and $\mu_{\mathrm{B}} = 9.3 \times 10^{-24}\,\mathrm{J\,T^{-1}}$ is the Bohr magneton. We would therefore expect a noticeable change in Γ_{NCF} if fluctuating electronic spins are responsible for it.

In Fig. S3, we show the line scans of frequency f and non-contact friction Γ_{NCF} as in Fig. 2 of the main paper. Figure S4(a) displays the dependency of the total cantilever dissipation Γ_{tot} on the external magnetic field far from the surface. We see that the cantilever damping increases with B, potentially due to magnetic impurities on the cantilever surface.

To test the surface dissipation added by the presence of the magnetic field, we extract the maxima and minima of the line scans of Γ_{NCF} in Fig. S3(c)-(d) and plot them versus d, see Fig. S5. For both materials, the data points agree with those for

$B = 0$ within the expected statistical spread. From these findings, we conclude that the dominant contribution to Γ_{NCF} over both materials must be assigned to electrical fluctuations that are independent of B.

Finally, we show in Fig. S6 the complementary plots to fig. 3(e)-(f) of the main text. As for $B = 0$, a clear correlation between Γ_{NCF} and f is apparent.

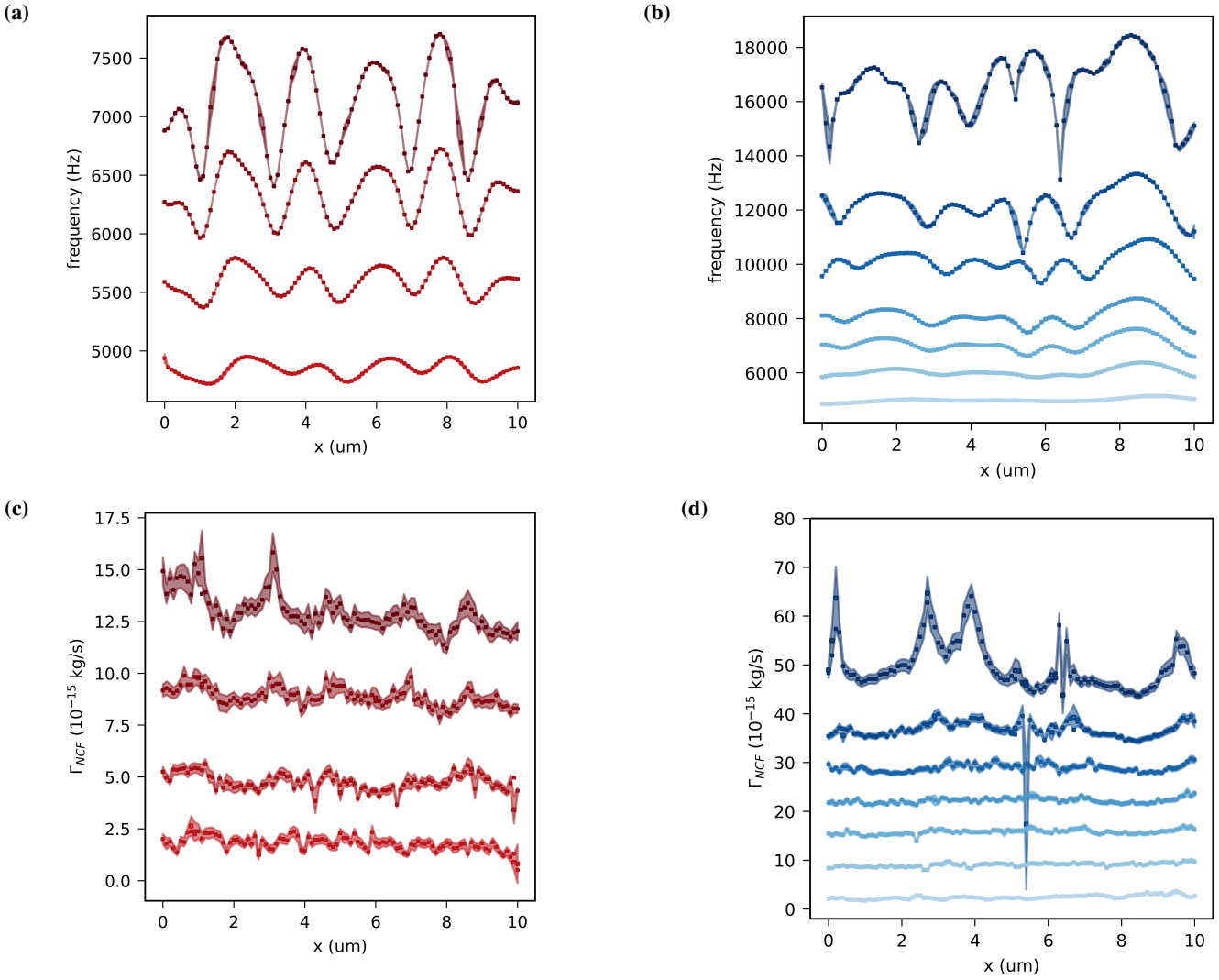

Figure S3: Line scans of the resonance frequency f and non-contact friction Γ_{NCF} over Au (a)-(c) and SiO_2 (b)-(d) under an external magnetic field of $4\,\mathrm{T}$ for $d = 20, 30, 45, 60\,\mathrm{nm}$ over Au and $d = 30, 45, 50, 70, 80, 100, 150\,\mathrm{nm}$ over SiO_2 (top to bottom). Lines are offset for better visibility by $0.075\,\mathrm{kHz}$ each in (a), 11, 7, 5, 3, 2, $1\,\mathrm{kHz}$ in (b), $3 \times 10^{-15}\,\mathrm{kg\,s^{-1}}$ each in (c), and $6 \times 10^{-15}\,\mathrm{kg\,s^{-1}}$ each in (d).

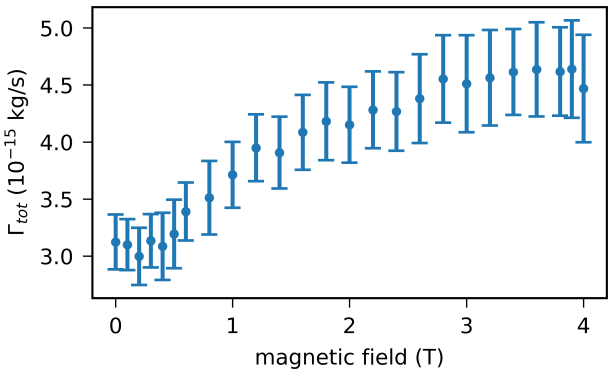

Figure S4: Dissipation Γ_{tot} as function of magnetic field far from the surface.

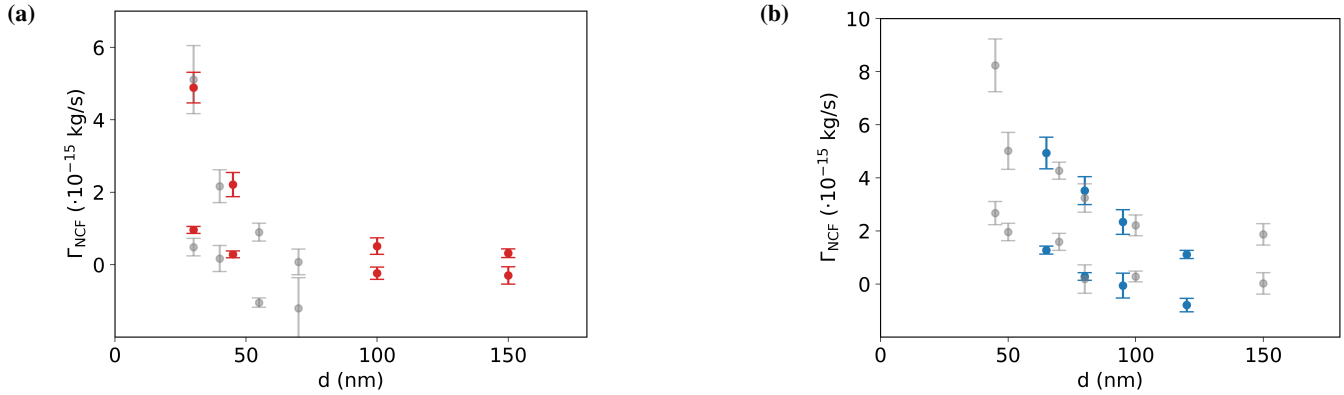

Figure S5: Maximum and minimum measured Γ_{NCF} under an external magnetic field of $4\,\mathrm{T}$ (grey data points). For comparison, the measured values without external field from Fig. 3 of the main manuscript are also shown (red, blue).

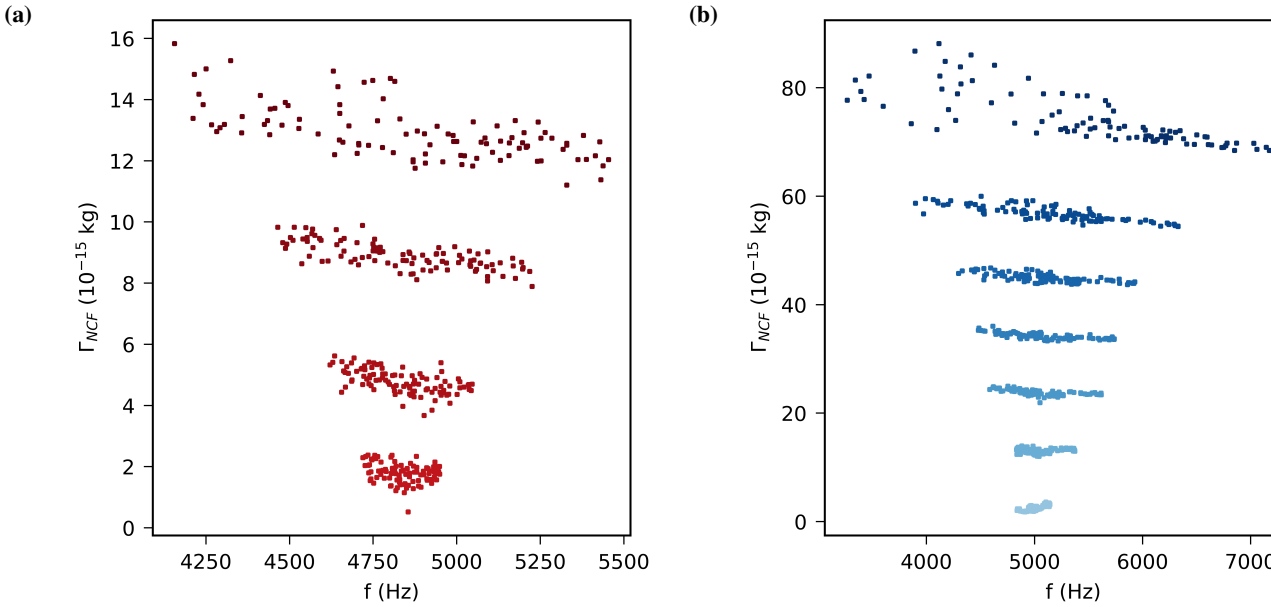

Figure S6: Γ_{NCF} as function of f in the presence of an external magnetic field of $4\,\mathrm{T}$ over Au (a) and over SiO_2 (b). Data are offset for better visibility by $3 \times 10^{-15}\,\mathrm{kg\,s^{-1}}$ each in (a), and $10 \times 10^{-15}\,\mathrm{kg\,s^{-1}}$ each in (b).

S4. CHARGE CALIBRATION

This section presents our calibration procedure to estimate the charge q_{tip} carried by the cantilever tip. We take advantage of the fact that our sample is a stripline used for inverting spins in magnetic resonance experiments [S4]. We apply a voltage to that stripline to electrostatically drive the cantilever vibrations. We then determine the force via the cantilever response function:

$$A(\omega) = \frac{F_d/m}{\sqrt{(\omega_0^2 - \omega^2)^2 + \left(\frac{\omega_0 \omega}{Q}\right)^2}} \tag{S4}$$

where $A(\omega)$ is the cantilever amplitude, F_d is the drive force, m and Q the cantilever's effective mass and quality factor, $\omega_0/2\pi = f_0$ its resonance frequency, and $\omega/2\pi$ the drive frequency. Measuring the amplitude at resonance, the force is therefore given by:

$$F_d = A(\omega_0) m \frac{\omega_0^2}{Q}. \tag{S5}$$

We simulate the electrical field $E_{\mathrm{sim}}(\mathbf{r})$ at a position $\mathbf{r} = (x, y, z)$ in COMSOL and use it to calculate the tip charge q_{tip} as

$$q_{\mathrm{tip}} = F_d(\mathbf{r})/E_{\mathrm{sim}}(\mathbf{r})\,. \tag{S6}$$

Note that the cantilever position must be carefully determined. When hovering over the stripline, we measure lateral shifts of several $10 - 100\,\mathrm{nm}$ compared to its nominal position, see Fig. S7(a). These shifts are monitored through changes in the feedback-controlled position of the cantilever in the interferometer fringe [S4]. We further found that the force values measured on both side of the stripline differ, which we ascribe to a potential difference between the cantilever tip and our setup ground. We managed to cancel this effect by applying a DC voltage of $1.6\,\mathrm{V}$ to the stripline, resulting in a symmetric response and an estimated charge number of $q_{\mathrm{tip}} \approx 20$.

Our method overestimates the number of charges interacting with the sample surface during the scanning force microscopy experiments. The Coulomb electric field of a point charge decays as $1/d^2$ whereas the driving field generated by the $\approx 2\,\mu\mathrm{m}$-broad stripline only starts to decrease as $1/d$ after a few micrometers. Our method therefore merely gives an upper boundary on the actual number of charges carried by the cantilever tip (within a few tens of nanometers from the apex).

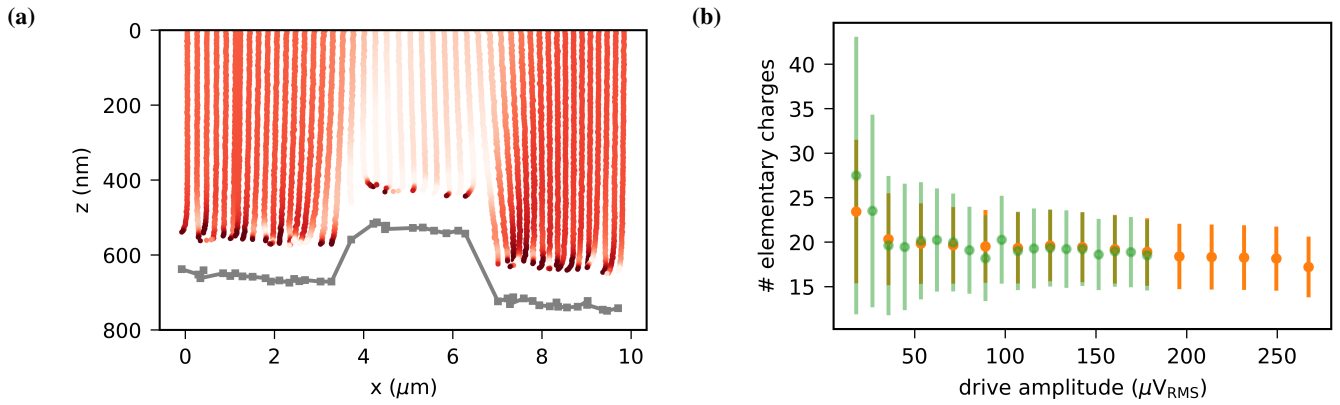

Figure S7: (a) Cantilever static shift (lateral shift) and frequency (color coded: dark red $4.5\,\mathrm{kHz}$, light red $5.5\,\mathrm{kHz}$) for successive approaches above the sample. Grey points indicate the cantilever touch positions. The stripline profile is clearly visible.
(b) Results of the charge calibration. The orange and green data is measured at the positions $x = 3.5\,\mu\mathrm{m}$ and $x = 6.5\,\mu\mathrm{m}$ in (a), respectively.

S5. ELECTROSTATIC MODEL

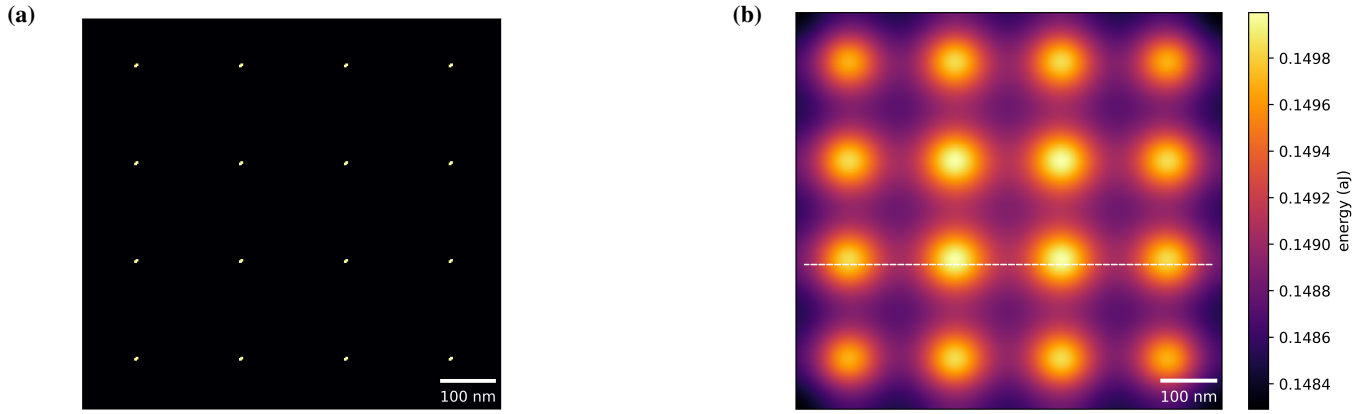

Figure S8: (a) Simple charge density model. A charge q_i is placed at each white dot. (b) Energy map corresponding to $q_{\mathrm{tip}} = q_e$ and $q_i = 0.7q_e$ at a surface-charge distance $d + \Delta = 50\,\mathrm{nm}$. The dashed line shows the position of the line scan in Fig. S9.

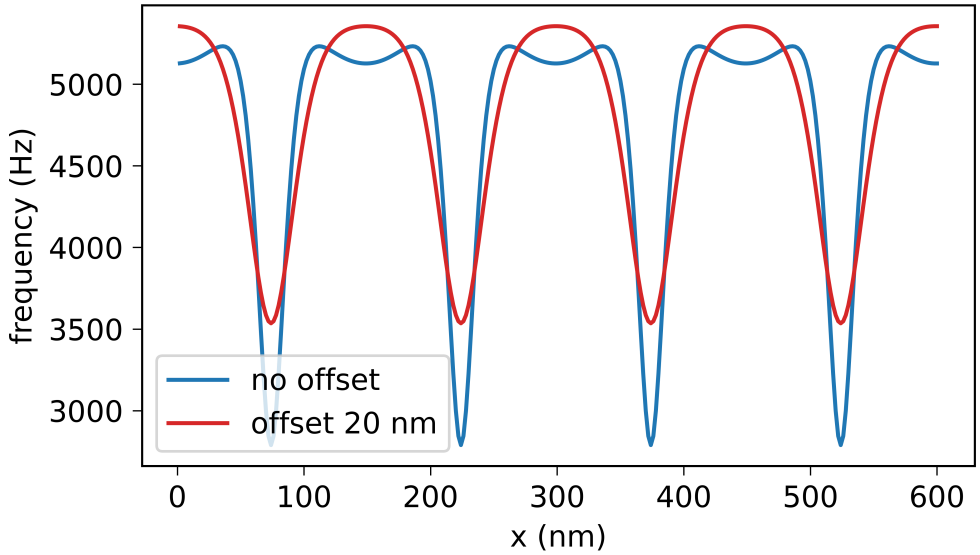

Figure S9: Calculated frequency along the white dashed line in Fig. S8(b). The result for $d = 30\,\mathrm{nm}$ without an offset is shown in blue, yielding a large asymmetry between the positive and negative frequency deviations and characteristic double maxima between charge sites that we do not observe in the experiment, cf. Fig 2(c) of the main text. Including a tip-charge offset of $\Delta = 20\,\mathrm{nm}$ results in a much more realistic simulation.

In the main text, we explain the simple electrostatic model used to calculate the variable frequency

$$f = \frac{1}{2\pi}\sqrt{\frac{k_0}{m} + \frac{k_{\mathrm{el}}}{m}}\,, \tag{S7}$$

where $k_{\mathrm{el}} = \delta^2 E_{\mathrm{el}}/\delta x^2$ is the electrical spring constant obtained from the summed Coulomb energy of charges q_i on the surface. For the model comparison in Fig. 3, we placed charges on a grid with a separation of $150\,\mathrm{nm}$, see Fig. S8. To avoid edge effects, we simulate a 10×10 times larger area than that shown (i.e., evaluated). Two free parameters are involved in this simulation: first, we fix the value of $q_{\mathrm{tip}}q_i = 0.7q_e^2$ by comparing the maximum and minimum frequencies found in a simulated line scan, see Fig. S9. Second, the characteristic asymmetry observed for $d = 30\,\mathrm{nm}$ over Au provides us with a criterion to estimate the offset Δ between the tip apex and the effective charge position. For $\Delta = 0$, the model corresponds to a charge placed at the very

apex, and the simulated line scan produces characteristic double peaks that are clearly absent in the experiment, see blue trace in Fig. S9. An offset of $\Delta = 20\,\mathrm{nm}$ ($\pm 5\,\mathrm{nm}$) removes these double peaks, while preserving the asymmetry between the sharp dips and the broad maxima, see red trace in Fig. S9. The asymmetry stems from the difference between placing the tip directly over a repulsive charge (frequency dip) or at a position between two charges (frequency maximum). The offset is comparable to the nanowire tip radius of $\sim 10\,\mathrm{nm}$ reported in an earlier publication [S5].

S6. SURFACE TOPOGRAPHY IMAGES

In Fig. S10, we display the surface topography of Au and SiO_2 on a second sample chip. The chip is cleaved from the same thermally oxidized Si wafer, and the Au layer was evaporated in the same process as for the sample mounted in out nanoladder scanning force microscope. The topography images in Fig. S10 were measured with a commercial atomic force microscope (AFM). They clearly show difference in topography between the two surfaces. In particular, the lateral grain sizes on Au are about $100 - 150\,\mathrm{nm}$ with a typical height of $4 - 6\,\mathrm{nm}$, while those on SiO_2 appear to be smaller, roughly $20 - 50\,\mathrm{nm}$ laterally and $1 - 1.5\,\mathrm{nm}$ high. From these differences, we conclude it unlikely that the very similar frequency maps in Fig. 2(a)-(b) of the main text are directly caused by topographic variations.

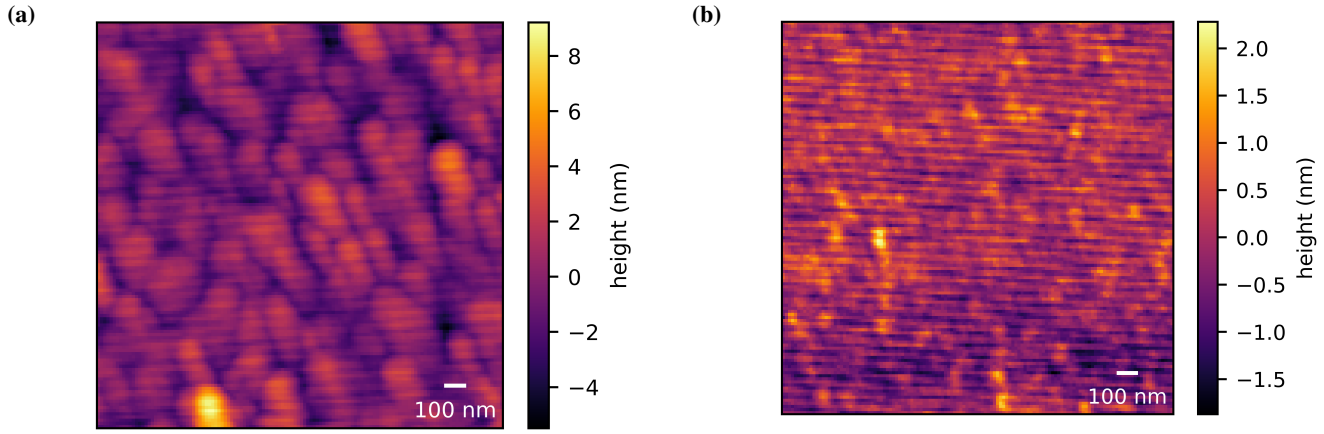

Figure S10: Surface topography of (a) Au and (b) SiO_2 surfaces on a second sample chip, measured with a commercial AFM.

S7. FREQUENCY MAP OVER A DIFFERENT SAMPLE

In a separate experiment, we measured the cantilever frequency f over a $3\,\mathrm{nm}$-thick Pt layer that was E-beam evaporated over diamond-like carbon, see Fig. S11. We observe a similar pattern as on Au and SiO_2, suggesting the presence of potential patches. We did not study the non-contact friction over this sample.

S8. XPS SAMPLE ANALYSIS

We performed X-ray photoelectron spectroscopy using a PHI Quantera SXM photoelectron spectrometer at the Swiss Federal Laboratories for Materials Science and Technology (EMPA), see Fig. S12. A monochromatic Al K_α X-ray source with a $100\,\mu\mathrm{m}$ circular spot size was used under ultrahigh vacuum ($1 \times 10^{-9}\,\mathrm{mbar}$). High-resolution C 1s spectra were acquired at a pass energy of $55\,\mathrm{eV}$ using a $20\,\mathrm{ms}$ dwell time. For all scans, $15\,\mathrm{kV}$ was applied with an emission current of $3\,\mathrm{mA}$; an average of 8-10 scans were collected per region. Spectra were fit with CasaXPS Software Version 2.3.23PR1.0 using a Shirley background and Gaussian-Lorenzian peak shapes to deconvolute contributions to the adventitious carbon signals. The dominant peaks were assigned to sp3 carbon and calibrated to $284.8\,\mathrm{eV}$ as a charge reference; satellite peaks at higher binding energies of ca. $+1.5\,\mathrm{eV}$ and circa $+3 - 4\,\mathrm{eV}$ were assigned to carbon singly and doubly bound to oxygen, respectively [S7]. Relative signal contributions were averaged over spectra collected from three distinct regions for both Au and SiO_2 surfaces.

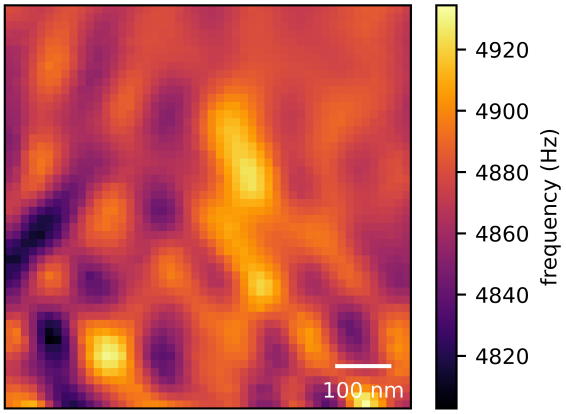

Figure S11: Frequency map measured $50\,\mathrm{nm}$ over Pt.

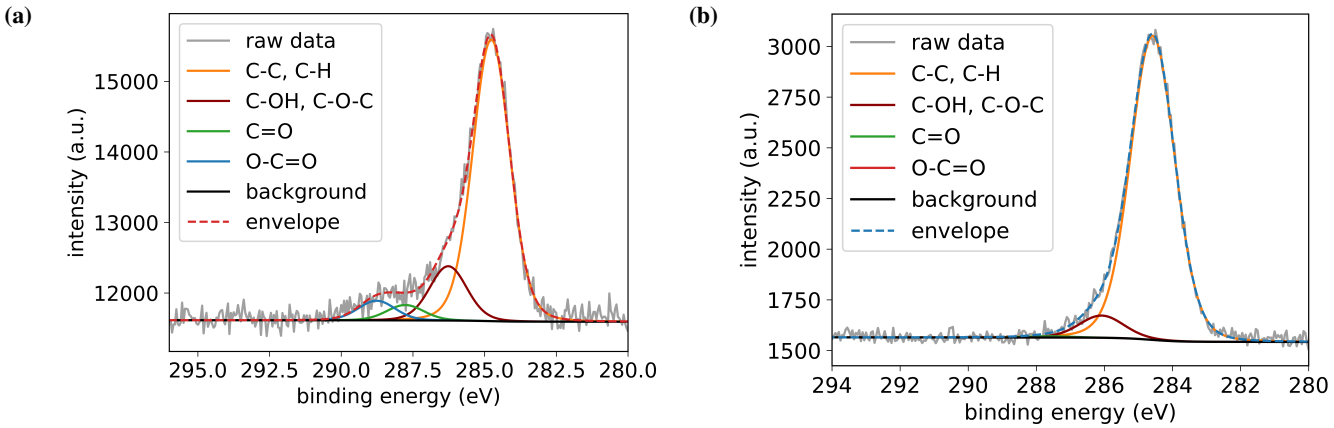

Figure S12: Representative X-ray photoelectron spectra of (a) Au and (b) SiO_2 surfaces showing high-resolution C 1s regions. The shape of the spectra indicate that the composition of adsorbed hydrocarbon contamination differ between Au and SiO_2 surfaces. Specifically, deconvolution of the C 1s signals suggests a greater contribution of C-O bonding character in the thin layers of adventitious carbon material present on Au compared to SiO_2. The non-identical nature of the adsorbed material can lead to different dielectric parameters due to the additional interaction of permanent dipole moments in polar, oxygen-containing species with electric fields [S6].

S9. ATTEMPT AT REMOVING THE ADSORBANT LAYER WITH MODERATE HEATING

In an exploratory effort to remove part of the adsorbant layer in situ, we modified the sample stage with a resistive heater and increased the sample temperature from $295\,\mathrm{K}$ to roughly $330\,\mathrm{K}$ for a few hours [S8]. The results of this test are summarized in Fig. S13.

Before heating, we measured the Q factor of the resonator at different tip-sample distances d. We then heated the sample stage, waited for several hours, and repeated the measurements, finding a significant increase of Q (and a reduction of Γ_{NCF}) relative to the untreated case. We then proceeded to cool down the system with the heater on, ensuring that the sample stage was always slightly warmer than its the surrounding parts of the cryostat. At our base temperature of roughly $4\,\mathrm{K}$, we found that Q and Γ_{NCF} were not significantly better than in the first cooldown without a heater. We speculate that the gas adsorption process during the cooldown was not sufficiently impeded by our weak heater, but further tests will be necessary to allow a solid interpretation of this result.

We emphasize that this preliminary series of measurements was not performed with the same stringent z-calibration procedure as the other data sets in our manuscript. The values of d in Fig. S13 are therefore only accurate to a few tens of nanometers. Similarly, the precise sample temperature achieved with our homebuilt heater is subject to an uncertainty. Indeed, the PT-1000 thermometer that measures the temperature at the sample stage has not been properly calibrated and only the reference point

of 295 K has been used. Nevertheless, the effect observed is large enough to conclude that the heater provoked a change of the resonator non-contact friction for distances up to several micrometers at room temperature.

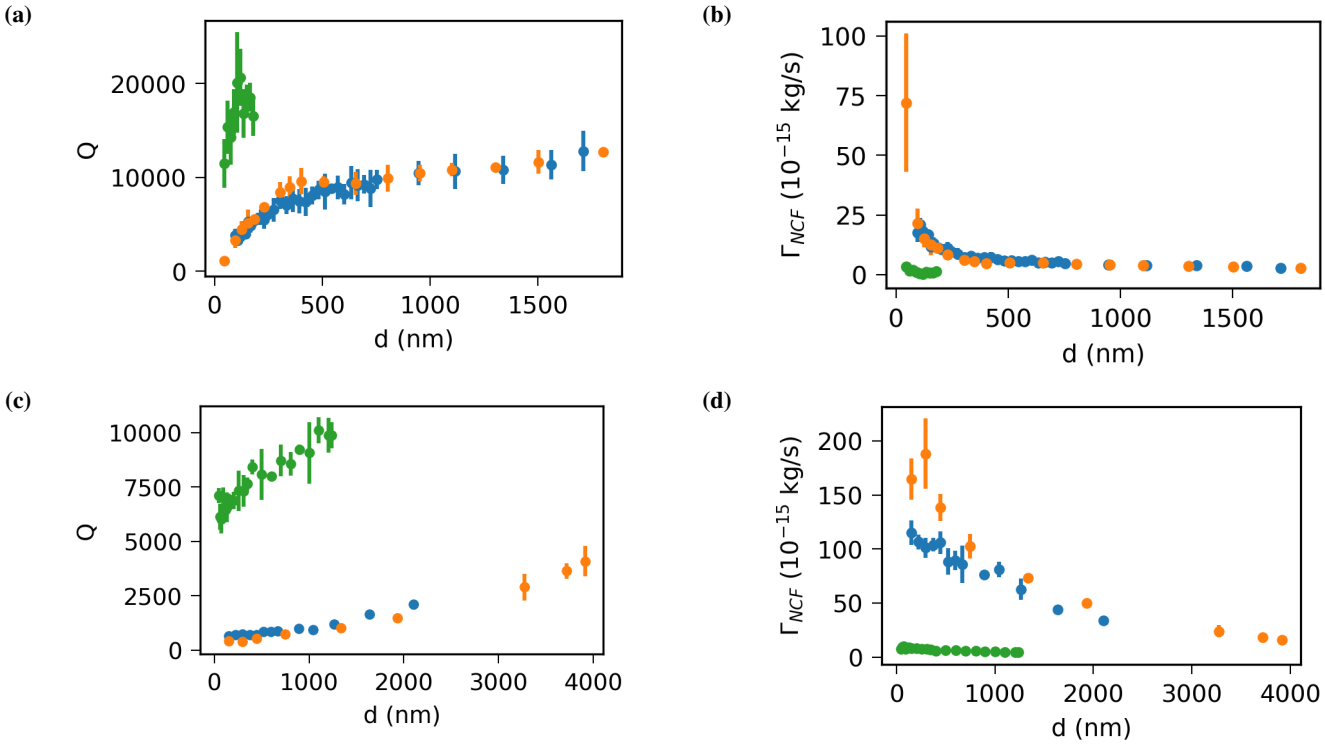

Figure S13: Effect of heating the sample with a resistive heater, from 295 K to roughly 330 K for a few hours. Blue data points were measured at room temperature. Green data were measured after having heated the sample for a few hours. Orange data show a second measurement at room temperature after turning off the heater. (a) and (b) show data measured over Au, while (c) and (d) were measured over SiO_2.

[S1] M. Héritier, A. Eichler, Y. Pan, U. Grob, I. Shorubalko, M. D. Krass, Y. Tao, and C. L. Degen, Nano Lett. **18**, 1814 (2018), ISSN 1530-6984.

[S2] S. M. Yazdanian, J. A. Marohn, and R. F. Loring, The Journal of Chemical Physics **128** (2008), ISSN 0021-9606, URL `https://www.ncbi.nlm.nih.gov/pmc/articles/PMC2674627/`.

[S3] S. Lekkala, J. A. Marohn, and R. F. Loring, The Journal of chemical physics **139**, 184702 (2013).

[S4] U. Grob, M. D. Krass, M. Héritier, R. Pachlatko, J. Rhensius, J. Košata, B. A. Moores, H. Takahashi, A. Eichler, and C. L. Degen, Nano Letters **19**, 7935 (2019), ISSN 1530-6984.

[S5] Y. Tao and C. L. Degen, Nano Letters **15**, 7893 (2015), ISSN 1530-6984.

[S6] A. D. Sen, V. G. Anicich, and T. Arakelian, Journal of Physics D: Applied Physics **25**, 516 (1992), URL `https://doi.org/10.1088/0022-3727/25/3/027`.

[S7] S. Sangtawesin, B. L. Dwyer, S. Srinivasan, J. J. Allred, L. V. H. Rodgers, K. De Greve, A. Stacey, N. Dontschuk, K. M. O'Donnell, D. Hu, et al., Phys. Rev. X **9**, 031052 (2019), URL `https://link.aps.org/doi/10.1103/PhysRevX.9.031052`.

[S8] D. Martinez-Martin, R. Longuinhos, J. G. Izquierdo, A. Marele, S. S. Alexandre, M. Jaafar, J. M. Gómez-Rodríguez, L. Bañares, J. M. Soler, and J. Gomez-Herrero, Carbon **61**, 33 (2013).